RSC Advances

PAPER

View Article Online
View Journal | View Issue

Cite this: *RSC Adv.*, 2025, **15**, 35436

Aramid and zirconia coated separator for enhanced electrochemical performance of lithium-ion batteries

Daofa Ying,* Kuo Chen, Jiazheng Lu, Chuanpina Wu, Baohui Chen, Yang Lv, Yutao Liu and Zhen Fang

Received 2nd June 2025
Accepted 3rd September 2025

DOI: 10.1039/d5ra03903g

rsc.li/rsc-advances

In this study, a novel porous composite separator was fabricated by depositing biomass-derived aramid-zirconia (AF-ZrO_2) on both sides of a commercial polyethylene (PE) separator. The influence of the aramid-zirconia coating on the properties of the resulting PE@AF-ZrO_2 composite separator was systematically investigated. The results demonstrate that the coating significantly enhances wettability, thermal stability, electrical insulation and mechanical properties relative to the pristine PE separator, resulting in enhanced electrochemical performance in both Li‖LiFePO4 coin cells and $LiFePO_4$‖graphite pouch cells. Specifically, the PE@AF-ZrO_2 composite separator exhibits an electrolyte uptake of 381%, an ionic conductivity of 0.306 mS cm^{-1}, a dielectric strength of 266 V μm^{-1} and a tensile strength of 189.5 Mpa. In Li‖LiFePO4 coin cells, the PE@AF-ZrO_2 separator delivers a discharge capacity of 128.2 mAh g^{-1} at a 10C discharge rate. Furthermore, $LiFePO_4$‖graphite pouch cells using the PE@AF-ZrO_2 separator show exceptional cycling stability, with 93.5% initial energy capacity retention after 1200 cycles. These results suggest that coating a PE separator with an aramid-zirconia layer represents an effective strategy to create a robust, high-performance composite separator, highlighting its promising commercial potential for lithium-ion batteries (LIBs).

1. Introduction

With the deepening global commitment to sustainable development, lithium-ion batteries (LIBs) have been widely adopted in electric vehicles, consumer electronics, and energy storage systems due to their environmentally friendly characteristics and high energy density.[1–4] A LIB cell consists of four primary components: a cathode, an anode, an electrolyte and a separator. While the separator does not participate in electrochemical reactions, it serves as a critical ionic conductor enabling Li^+ transport between electrodes while maintaining electrical insulation.[5] The physicochemical properties of separators-including porosity, thermal stability and mechanical strength-profoundly influence the cell's cycle life, rate capability and safety performance.[6] For instance, inadequate thermal stability can lead to separator shrinkage or meltdown at elevated temperatures, increasing the risk of internal short circuits and thermal runaway. Similarly, non-uniform pore architecture may restrict ion mobility, reducing ionic conductivity and rate capability.[7] Consequently, designing safe, mechanically robust separators with optimized pore structure and surface functionality (enhanced wettability, lithium dendrite resistance) remains pivotal for advancing next-generation high-safety LIBs.

Currently, commercial lithium-ion battery (LIB) separators are predominantly composed of petroleum-derived porous membranes, such as polyethylene (PE) or polypropylene (PP). These materials are widely used due to their cost-effectiveness, ease of fabrication, stable electrochemical windows (voltage tolerance >4.3 V *vs.* Li/Li^+) and robust mechanical properties (tensile strength >100 MPa). However, their inherent hydrophobicity leads to poor electrolyte wettability, which adversely impacts ion transport kinetics, resulting in diminished rate capability and cycling stability. Furthermore, their limited thermal stability (softening temperatures <150 °C) poses significant safety risks, as separator shrinkage or meltdown at elevated temperatures can trigger internal short circuits and thermal runaway.

To address these limitations, functional coating strategies have emerged as economically viable solutions.[8] For instance, polar polymer coatings including polymethyl methacrylate (PMMA), polydopamine (PDA), and polyacrylic acid (PAA) have been applied to PE-based separators to enhance surface hydrophilicity and electrolyte uptake. While these modifications improve wettability, their low thermal resistance (*e.g.*, 30% shrinkage at 150 °C) and porosity reduction (due to polymer filling of pores) create a performance trade-off, ultimately

---

State Key Laboratory of Disaster Prevention and Reduction for Power Grid Transmission and Distribution Equipment, State Grid Hunan Electric Company Limited Disaster Prevention and Reduction Center, Changsha, Hunan, P.R. China. E-mail: 17364041396@163.com; Tel: +86-0731-86332056

limiting their practicality for high-temperature applications. In addition, pure polymer-coated separators offer limited improvement in the separator's impact resistance, fail to effectively inhibit lithium dendrite penetration, and thus pose a high risk of internal short circuits in batteries. Therefore, composite inorganic material (*e.g.*, attapulgite (ATP) nanofibers,[9] SiO_2,[10] Al_2O_3,[11] TiO_2 [12] and BN nanoshheets[13] and BN nanotube[14]) with high thermal stability and hardness have emerged as a simple yet efficient solution. Moreover, some ceramic coating strategies have already become large-scale commercialized products.

Zirconia and aramid both possess excellent thermal stability and flame retardancy, as well as high electrical strength[15,16]—properties that make them promising candidates for enhancing the performance and safety of battery separators. While zirconium dioxide (ZrO_2) has recently garnered attention for improving cycling stability in sodium-ion batteries,[17] its synergistic effect with biomass-derived aramid in lithium-ion battery (LIB) separators remains largely underexplored. Herein, we design a novel porous composite separator comprising biomass-derived aramid particles and nanoscale ZrO_2, aiming to leverage the complementary advantages of both materials. We systematically characterize the separator's thermal (*e.g.*, thermal shrinkage) and electrical (*e.g.*, ionic conductivity, breakdown strength) properties, and investigate its role in LIB performance—specifically, its impact on electrolyte wettability, ionic transport uniformity. The electrochemical performance of cells employing the aramid-ZrO_2 composite separator is benchmarked against bare PE separator, with emphasis on rate capability and cycle life.

2. Experimental sections

2.1. Synthesis of biomass-based aramid and ZrO_2 coated separator

A separator coating slurry was prepared by thoroughly dispersing 2.55 kg of 10% solid-content bio-based aramid (the biomass-based aramid nanofiber suspension is sourced from Anhui Like New Material Technology Co., Ltd), 4.81 kg of zirconium oxide (ZrO_2), 0.38 kg of 2% carboxymethyl cellulose (CMC) solution, and 0.98 kg of polyacrylic acid (40 wt% PAA) binder into 6.23 kg of deionized water using a high-speed disperser. Subsequently, the slurry was applied to both sides (A and B) of the separator using a gravure coater, with the dried coating thickness controlled to 2 μm per side (A/B). The resulting aramid-zirconium oxide coated separator was designated as PE@AF-ZrO_2.

2.2. Characterizations

Morphology information was obtained *via* scanning electron microscopy (Zeiss, SIG-MA). Powder XRD analysis was performed using X-ray diffraction (Rigaku Miniflex600) with Cu@Ka radiation. Fourier transform infrared spectroscopy was acquired using a FTIR5700 spectrometer. The contact angles (CAs) and electrolyte wetting rate of different separators were measured *via* the sessile drop using an optical contact angle analyzer instrument (SDC-350KS, KRUSS). Nitrogen adsorption–desorption measurements were conducted with degassing at 105 °C for 12 h (full pore mode), and pore size distribution was derived from the desorption branch using the BJH method. The tensile strength, puncture strength and peel strength of the separator samples were measured using a Sans universal testing machine, and the testing protocols followed national standards.

The peel strength of zirconia ceramic-coated separators was tested following ASTM D903-1. The peel strength (P) was determined using the formula:

$$P = \frac{F_{\text{avg}}}{W} \quad (1)$$

where P is peel strength, F_{avg} is the average peel force, W is the sample width.

The electrolyte uptake (n) of separator samples were calculated with following formula:[18]

$$n = \frac{W_1 - W_0}{W_0} \times 100\% \quad (2)$$

where W_0 and W_1 are the weights of the separators before and after absorption of the liquid electrolyte.

For dielectric strength testing, three 10 cm × 10 cm samples of each separator type were prepared. Breakdown voltage measurements were performed using a JB7120 dielectric strength tester (Dongguan Guangxin Electronics Technology Co., Ltd). During each test, the separator was clamped between parallel copper cylindrical electrodes (diameter: 50 mm) under direct current (DC) mode. The voltage was ramped at a constant rate of 100 V s^{-1} until the leakage current exceeded 1 mA, at which point the instantaneous voltage was recorded as the breakdown voltage. The dielectric strength was then calculated according to formula (3):

$$E = \frac{U}{d} \quad (3)$$

where E is dielectric strength, U is breakdown voltage, d is the thickness of tested separator.

Electrochemical impedance spectroscopy (EIS), Cyclic voltammetry (CV) and linear sweep voltammetry (LSV) of the button cells assembled with bare PE and PE@AF-ZrO_2 separator were tested by CHI670 (Shanghai Chenhua Instrument, China) electrochemical workstation. The ionic conductivity was measured by sandwiching the separator samples between two stainless-steel (SS) blocking electrodes at 0.1 MHz–0.1 Hz. The values were calculated with fomula (4):

$$\sigma = \frac{d}{R_b \times S} \quad (4)$$

where σ is ionic conductivity, d is the thickness of separator, R_b is the bulk resistance and S is the surface area of the separator.[4]

2.2.1 Coin cell evaluation. The $LiFePO_4$ cathode for Li‖separator‖$LiFePO_4$ coin cells was fabricated by homogenizing active material, acetylene black, and polyvinylidene fluoride (PVDF) in an 8 : 1 : 1 weight ratio within *N*-methyl-2-pyrrolidone (NMP) solven. The slurry was blade-coated onto 15 μm double-sided carbon-coated aluminum foil (1 μm carbon layer per side), yielding an active material areal loading of 7 mg cm^{-2} and electrode thickness of 75 ± 1 μm. CR2032 coin cells were assembled in an argon-filled glovebox (<0.1 ppm O_2/H_2O) using lithium foil counter electrodes, a 16-mm-diameter separator, and 1 M $LiPF_6$ in EC/DEC/DMC (1 : 1 : 1 v/v) electrolyte. Cycling performance was evaluated *via* constant current charge–discharge tests (LAND CT3002A testing system, 2.5 to 3.7 V). C-rate capability was assessed by cycling at discharge currents of 0.2, 0.5, 2.0, 5.0, and 10.0C, with charging fixed at 0.2C for rate tests and 5.0C for cycle tests (discharge current matched charge current).

2.2.2 Pouch full-cell evaluation. For cathode fabrication, a slurry comprising 25 kg of $LiFePO_4$ (LFP)/carbon black/PVDF/ and carbon nanotubes (95.5 : 2 : 2 : 0.5 wt%) was dispersed in *N*-methyl-2-pyrrolidone (NMP) and homogenized, this slurry was slot-die coated onto both sides of 15 μm carbon-coated aluminum foil to achieve an active material loading of 32.4 mg cm^{-2}. Followed by calendereing to a compaction density of 2.6 g cm^{-3}. For anode preparation, 15 kg of graphite/ carboxymethyl cellulose/carbon black/aqueous binder/styrene-butadiene rubber (96.00 : 0.8 : 1 : 1.2 : 1 wt%) was dispersed in deionized water, coated onto 8 μm copper foil at 15.5 mg cm^{-2} loading, and calendered to 1.0 g cm^{-3} compaction density. After tab-cutting, the electrodes and separator were stacked into 1.7 Ah pouch cells (N/P ratio: 1.25), and injected with 1 M $LiPF_6$ in EMC/VC/EC/PC (49.74 : 2.5 : 29.86 : 5 : 12.9 wt%) at 5 g Ah^{-1}. Cells underwent formation at 200 mA to 20% state of charge (SOC), followed by constant-current charging at 850 mA to 100% SOC. All subsequent performance tests employed a 0.5C charge/ 0.5C discharge protocol.

3. Results and discussion

Fig. 1a displays XRD patterns of ZrO_2, bare PE separator and the modified PE@AF-ZrO_2. Compared to bare PE separator, the PE@AF-ZrO_2 pattern exhibits new characteristic peaks centered at approximately 28.2° and 31.7°. These peaks are consistent with the ZrO_2 reference pattern (PDF#37-1484), indicating that ZrO_2 was successfully coated on the bare PE separator. Infrared spectroscopy is commonly used to identify substances through characteristic functional groups. Attenuated total reflectance-Fourier transform infrared (ATR-FTIR) spectra were collected for both PE and PE@AF-ZrO_2 (Fig. 1b). Compared to the PE spectrum, the PE@AF-ZrO_2 spectra shows new absorption peaks at 3058, 1668, 1514 cm^{-1}. These peaks indicate the presence of amide and heterocyclic ring groups, specifically assigned to N–H stretching, C=O stretching, C=C skeleton vibration respectively. Furthermore, a peak at 580 cm^{-1} assigned to Zr–O stretching, was also detected in PE@AF-ZrO_2. Therefore, a biomass based aramid-zirconia-coated separator was successfully prepared.

As shown in Fig. S1a, the separator substrate used in this study exhibits a nanofiber-constructed porous structure, consistent with typical characteristics of wet-processed separators. Fig. S1b provides atomic force microscopy (AFM) images that further unequivocally demonstrate this porous architecture. The corresponding height image (Fig. S1c) verifies excellent height uniformity of the substrate, with a calculated surface roughness of merely 23 nm. Fig. S2a and S2b present the morphological image and height image, respectively, of the biomass-based aramid nanofibers employed in this study, demonstrating nanoscale dimensional uniformity. The arithmetic mean roughness (Ra) of these biomass aramid fibers is quantified at 61.1 nm (measured over a 2 × 2 μm scan area). Fig. S3a and S3b present scanning electron microscopy (SEM) images of the zirconia (ZrO_2) particles employed in this study at magnifications of 2000× and 5000×, respectively. The results demonstrate that the ZrO_2 particles exhibit an average particle size of approximately 300 nm, this particle size facilitates the formation of an ultrathin coating while maximizing pore structure retention. Fig. 2a and b presents the front side and back side images of PE@AF-ZrO_2. Both sides exhibit similar morphologies. Enlarged images (Fig. S4a and b) reveak uniform pores are formed by the accumulation of zirconia and aramid nanofibers, with consistent pore distribution and morphological features on both side, confirming structural uniformity. As shown in the Fig. S5, no obvious defects are observed at coating-substrate interface, indicating good interfacial bonding between the biomass-based aramid-ZrO_2 coating and the base separator. Furthermore, we measured the peel strength of the coating using a peel force tester (peel speed: 500 mm s^{-1}). The PE@AF-ZrO_2 separator exhibited peel strengths exceeding

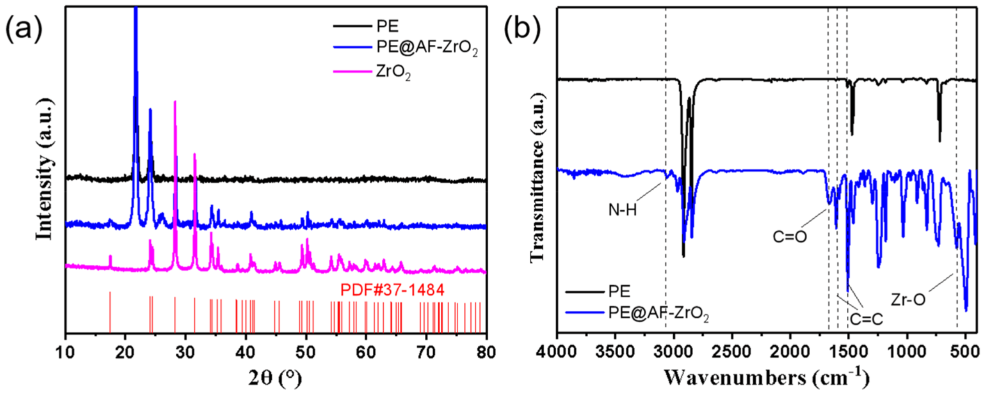

Fig. 1 (a) XRD patterns of PE, PE@AF-ZrO_2 separator and ZrO_2 particles, (b) ATR-FTIR spectra of PE and PE@AF-ZrO_2 separator.

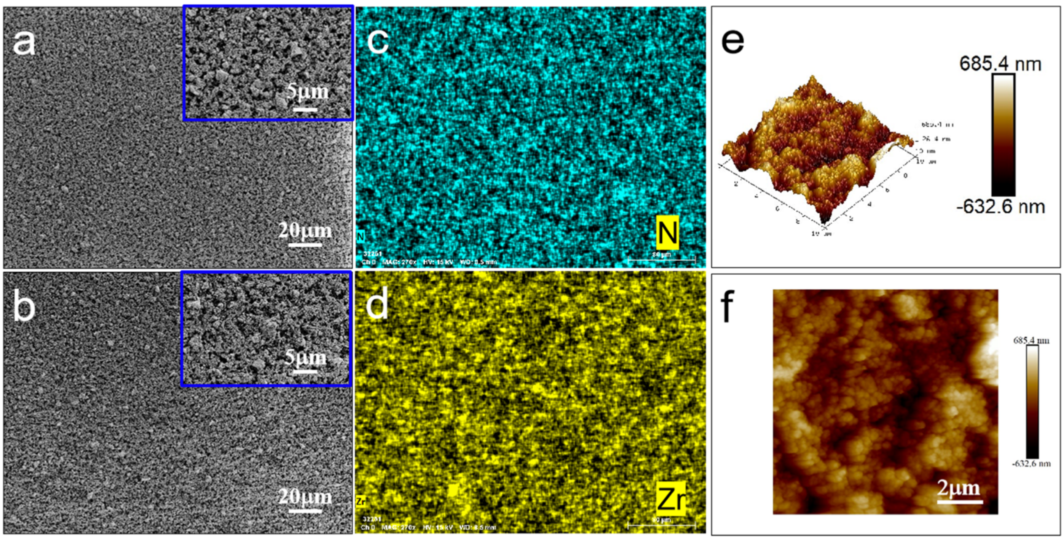

Fig. 2 SEM images of PE@AF-ZrO$_2$, (a) front side, (b)back side, (c) N element mappin, (d) Zr element mapping of PE@AF-ZrO$_2$, (e) AFM height image and (f) morphologyof PE@AF-ZrO$_2$.

exceeded 400 N m^{-1}, with 423.2 N m^{-1} for side A and 451.3 N m^{-1} for side B, which is over 2-fold higher than conventional ceramic separators (typically 100–200 N m^{-1}), these results clearly demonstrate that the biomass-based aramid-ZrO$_2$ coating bonds tightly with the base separator. Energy-dispersive X-ray spectroscopy (EDS) confirms the uniform distribution of zirconia and aramid particles throughout the PE@AF-ZrO$_2$ separator (Fig. 2c and d), and the atomic ratio content of N and Zr element has reached 7.35% and 11.45%, respectively (Fig. S8). Fig. 2e shows AFM height image of PE@AF-ZrO$_2$, with a surface roughness (Ra) value of 146 nm, indicating high flatness. Similarly, Fig. 2f demonstrates the presence of a porous structure on the PE@AF-ZrO$_2$ surface. Collectively, these characterization results confirm that the PE@AF-ZrO$_2$ separator maintains excellent surface uniformity and structural consistency, with a well-integrated coating, uniform particle distribution, and preserved porous architecture.

The thermal stability and electrical insulation of the coated separators were assessed. Fig. 3a illustrates photographs of bare PE, PE@AF-ZrO$_2$ separator samples after being exposed to certain temperatures for 1 h. The bare PE separator experienced initial shrinkage at 100 °C, with significant wrinkles forming at 130 °C, indicating pronounced contraction, when the temperature reached 150 °C, the bare separator was barely observable. In contrast, the coated separators exhibited improved thermal stability. Even after being exposed to 150 °C for 1 h, the PE@AF-ZrO$_2$ separator retained approximately 50% of its initial area. This demonstrates that the zirconia-containing coating effectively enhanced the thermal stability of the PE separator. The electrical strength of a separator also significantly impact on the manufacturing process and safety of lithium-ion batteries. PE@AF-ZrO$_2$ exhibitsed breakdown voltage of 3.46 kV, which is 5.7 times to the bare PE separator (Fig. 3b). The corresponding dielectric strength was 266 V μm^{-1}, representing a 300% increase compared to the bare PE separator (Fig. 3c). This improvement is attributed to the excellent insulating properties of both aramid and zirconia, which are evenly assembled on the surface of the base separator. The mechanical properties of the separator are closely related to the cycling performance of lithium-ion batteries.[19] As shown in Fig. 3d, The tensile strength of PE@AF-ZrO$_2$ reaches 189.5 MPa, which is increased by 23% compared to that of the bare PE separator (154.3 MPa), while the breaking elongation remains at 53.7%. The puncture force increased from 0.48 kgf (before coating) to 0.58 kgf (after coating) (Fig. 3e), representing an approximate 21% improvement. The mechanical enhancement is attributed to the reinforcing effect of aramid fibers, which form a 3D network that resists tensile deformation, the improvement in puncture resistance is due to the ZrO$_2$ coating, which increases the separator's surface hardness and can provides a physical barrier against lithium dendrite penetration. Together, these properties ensure the separator can withstand both mechanical stress (*e.g.*, cell expansion) and electrochemical threats (*e.g.*, lithium dendrites), thereby improving battery performance (cycle life) and safety (preventing short circuits).

Fig. 4a and b depict the contact angles of the electrolyte on bare PE and PE@AF-ZrO$_2$ separator samples. The inherent hydrophobic nature of bare PE results in a relatively high contact angle of 28.38°. Notably, the contact angle on coated separators significantly decreases, reaching 7.57° for PE@AF-ZrO$_2$. As shown in Fig. 2, the coated separator surface is covered with the coating materials, indicating the development of relatively smaller pores. As shown in Fig. S7a, the coated separator (PE@AF-ZrO$_2$) exhibited reduced adsorbed volume compared to the pristine PE, attributable to partial pore blocking by the aramid-ZrO$_2$ coating. Consequently, the Gurley value increased from approximately 89.7 to 134.6 s (Fig. 4c). However, Fig. S7b further reveals that both separators maintain a monomodal pore size distribution, with the average pore size increasing from 32 nm (pristine PE) to 45 nm (PE@AF-ZrO$_2$),

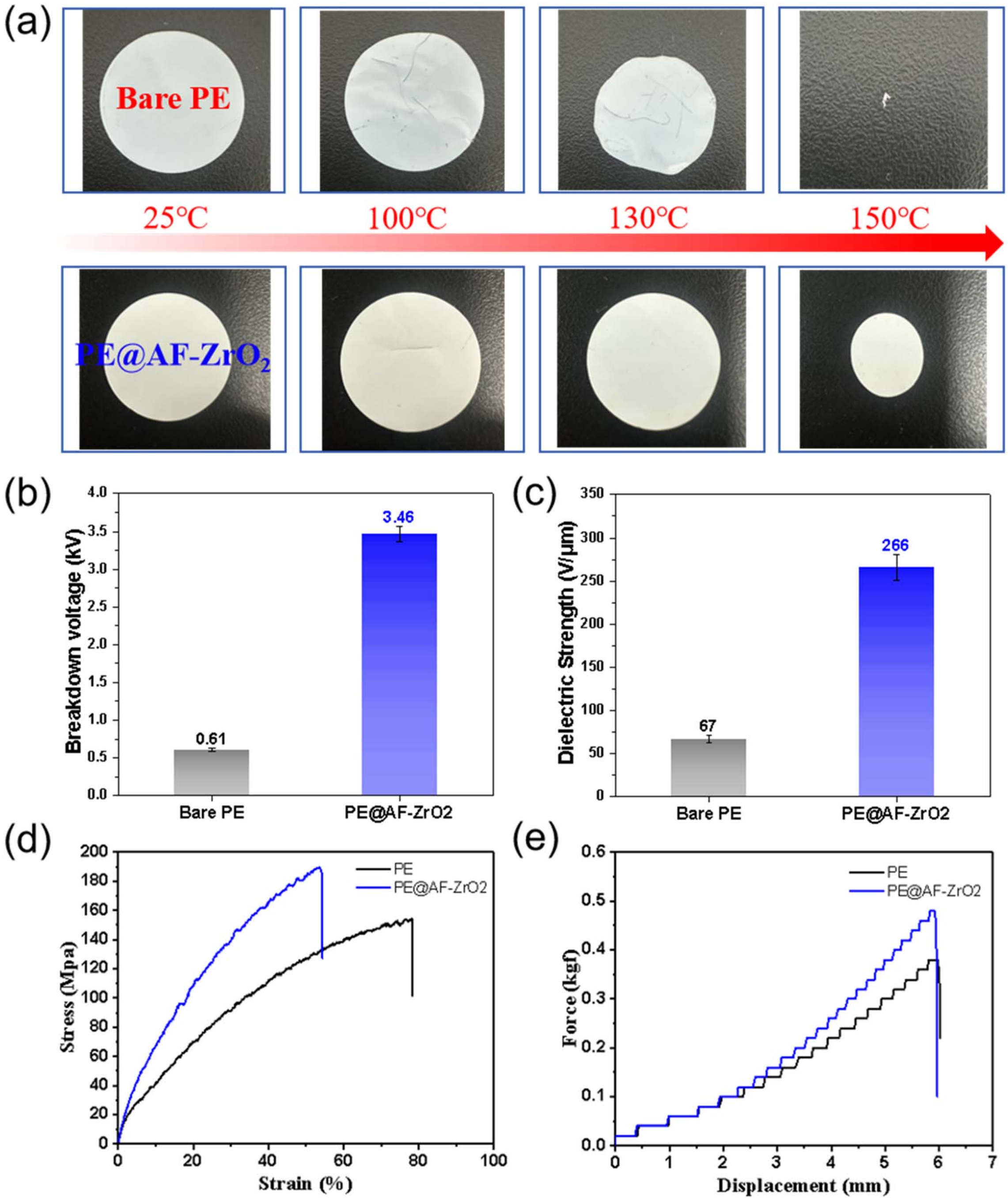

Fig. 3 (a) Digital image of the PE and PE@AF-ZrO_2 composite separators after thermal treatment at 25, 100, 130 and 150 °C for 1 h, (b) breakdown voltage, (c) dielectric strength, (d) stress–strain curves and (e) force-displacement curves in puncture strength test of bare PE and PE@AF-ZrO_2 separator.

due to well-defined pores within the coating layer and improved electrolyte wettability, electrolyte uptake in the PE@AF-ZrO_2 separator significantly increased to 371%, compared withe that of the bare PE separator (197%) (Fig. 4d). Additionally, aramid and zirconia-modified separators exhibit a significantly enhanced electrolyte wetting rate. The PE@AF-ZrO_2 separator achieves complete electrolyte wetting in only ~3 seconds, whereas the bare PE separator fails to achieve complete wetting even within 60 seconds (Video S9a and b). Combined with the porous structure characterized in Fig. 2 (uniform interparticle pores generated by ZrO_2 particle stacking) and the enhanced electrolyte wettability presented in Fig. 4, these structural and interfacial features synergistically facilitate rapid Li migration within the electrolyte-filled pores of the separator.[17,20]

The primary role of the separator is to prevent direct contact between the anode and cathode while facilitating effective Li-ion transport through the electrolyte. The ion transport resistance in a battery includes separator's bulk resistance and the interfacial

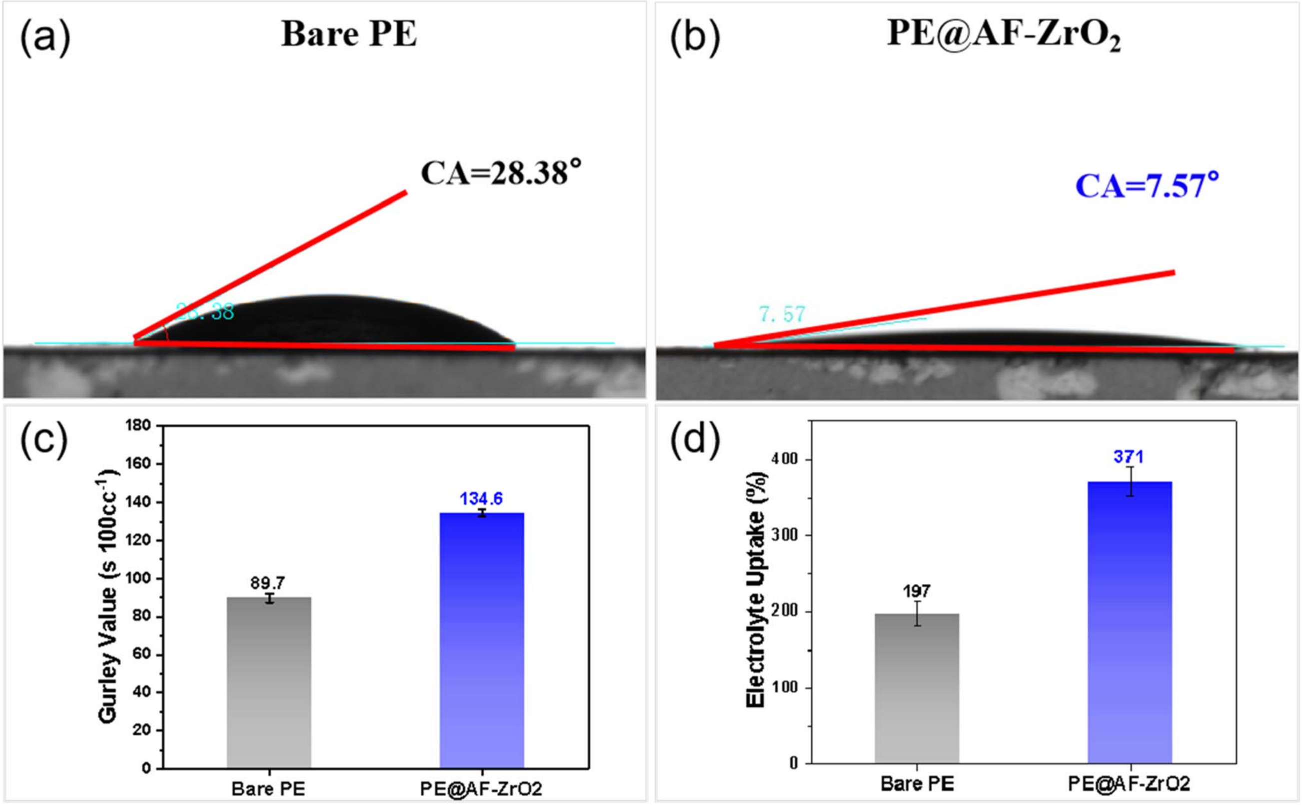

Fig. 4 (a) Contact angles of electrolyte on bare PE separator, (b) PE@AF-ZrO_2 separator, (c) Gurley value and (d) electrolyte uptake capacities of PE separator and PE@AF-ZrO_2.

resistance between the separator and electrode sheets. A lower interfacial resistance favors Li-ion intercalation/deintercalation at electrodes and is a critical performance indicator for battery separators. The interface resistances of the two separators were measured *via* AC impedance spectroscopy on Li/separator/Li blocking cells. As present in Fig. 5a,the interface resistance of PE@AF-ZrO_2 is 297 Ω, much lower than that of bare PE (533 Ω). This is because the coated modified separator has better wettability than the bare separator, thereby reducing the ion transport resistance at the separator–electrode interface. The bulk resistance of bare PE and PE@AF-ZrO_2 separators were characterized by EIS (Fig. 5b), yielding values of 1.66 Ω and 3.08 Ω, respectively. Based on these results, the ionic conductivity of PE@AF-ZrO_2 separator was measured, reached to 0.306 mS cm^{-1}, representing a 170% increase compared to bare PE (0.114 mS cm^{-1}). Under normal conditions, Li^+ in the electrolyte is solvated by strongly polar organic solvents (*e.g.*, EC), forming a large solvent sheath.[4,21] This limits the concentration and *trans*-membrane migration of free Li^+ in the electrolyte, potentially causing inefficient transport of PF^{-6} anions and further issues such as concentration polarization, lithium dendrite growth and thermal runaway.[22] The enhanced Li-ion conductivity may be attributed to the presence of zirconia and biomass-based aramid, which significantly increase the surface polarity of the separator. Furthermore, Cyclic voltammetry (CV) was used to evaluate the influence of the separator's influence on charge–discharge polarization. As shown in Fig. 5c, the oxidation potential of PE@AF-ZrO_2 is 3.626 V, lower than that of bare PE separator (3.665 V). This indicates that when PE@AF-ZrO_2 is used as the separator, the battery exhibits lower polarization, requiring a lower charging potential. The reduction potential of PE@AF-ZrO_2 is approximately 3.258 V, significantly higher than that of bare PE separator (3.180 V). The redox potential differences between the two separators are 0.49 V and 0.36 V, respectively. These results clearly show that batteries assembled with PE@AF-ZrO_2 exhibit a higher discharge voltage and lower polarization compared to those with bare PE. Additionally, both separators show symmetric redox peaks in CV curves, indicating good charge–discharge reversibility for Li-ion batteries.

Encouraged by the improved electrochemical performance of the coated separators, LFP/Li cells with various separator samples were assembled, and their electrochemical performance was investigated. As depicted in Fig. 5d, the cell assembled with PE@AF-ZrO_2 delivers 164.8 mAh g^{-1}, which is notably higher than that of the cell with bare PE (161.3 mAh g^{-1}). It can also be observed that cell assembled with PE@AF-ZrO_2 exhibits better performance than the bare PE separator cell at all discharge rates and under all conditions. Specifically, as the discharge rate increases, the performance gap gradually widens. When the rate reachs 10C, the gap maximized: the discharge specific capacity of cell wih PE@AF-ZrO_2 still retains 128.2 mAh g^{-1}, whereas that of the bare PE cell wih bare PE is120.5 mA g^{-1}. This can be attributed to the coating's effective reduction of battery polarization under high-rate conditions. The cycle stability of cells wiht different separators was also

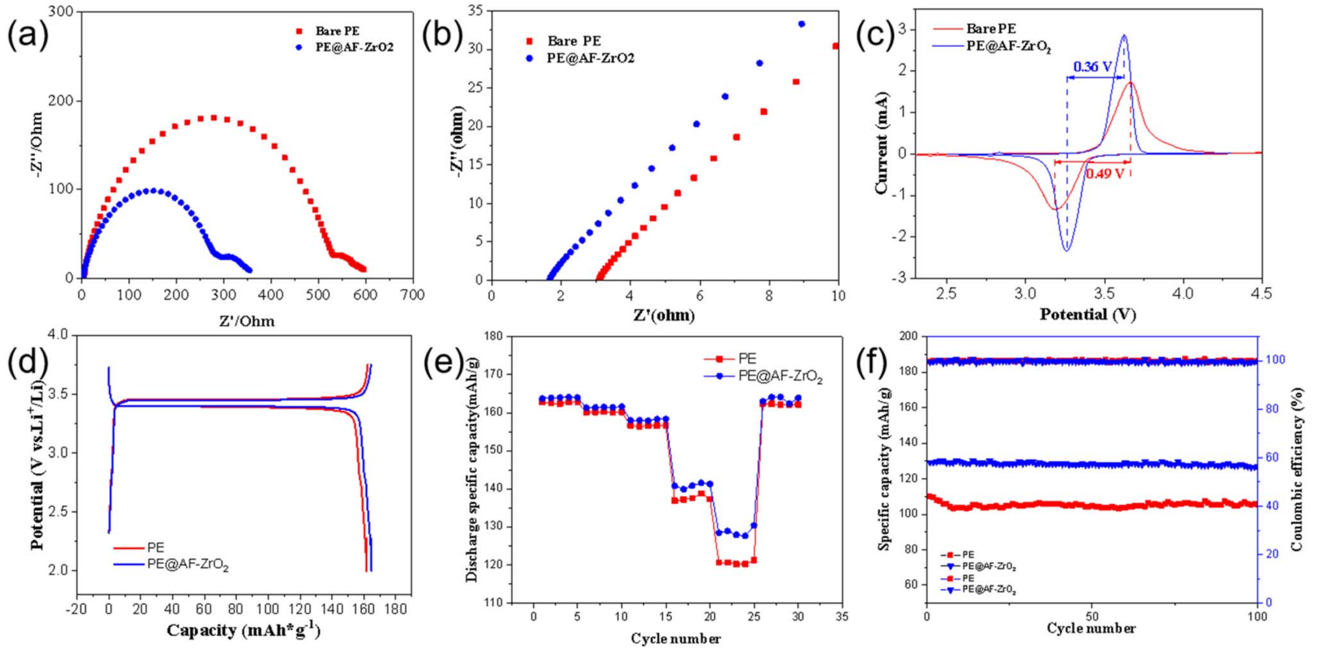

Fig. 5 (a) Electrochemical impedance spectra of Li/separator/Li cells with bare PE and PE@AF-ZrO$_2$ separator, (b) Nyquist plots of steel/separator/steel cells assembled with bare PE and PE@AF-ZrO$_2$ separator, (c) the cyclic voltammetry curve of the LiFePO$_4$/separator/Li cells, (d) initial charge/discharge curves of bare PE and PE@AF-ZrO$_2$ separator, (e) rate performances of LiFePO$_4$/separator/Li cell, (f) cycling performances of LiFePO$_4$/separator/Li cells at 0.5C at 25 °C.

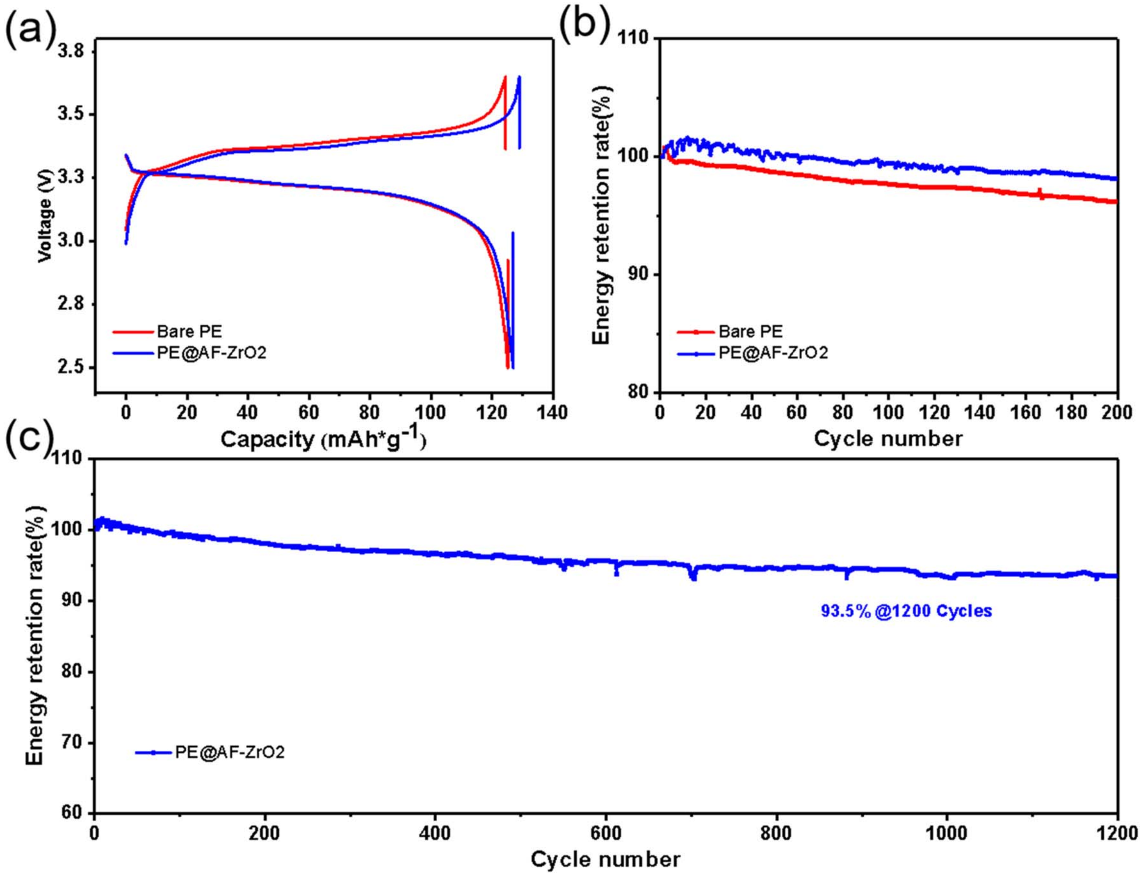

Fig. 6 (a) Charge–discharge curves, (b) cycling performance at 0.5C in a range of 2.5–3.65 V of LFP‖graphite pouch cell assembled with bare PE and PE@AF-ZrO$_2$ separator, (c) 1200 cycles performance of pouch cell with PE@AF-ZrO$_2$.

evaluted. Fig. 5f illustraes the capacity retention of cells using bare PE and PE@AF-ZrO_2 separators under 5C charge 5C dicscharge conditions. The cell with PE@AF-ZrO_2 shows slow specific capacity decay over 100 repetitive charge–discharge cycles, whereas the bare PE cell undergoes rapid capacity fading during the first 10 cycles. This indicates significantly improved cycle stability for the cell with PE@AF-ZrO_2 compared to the bare PE cell.

The practical application of the composite separator was further evaluated by testing in pouch cell. Pouch cell equipped with PE@AF-ZrO_2 exhibit smoother charge–discharge curves compared to control (Fig. 6a). This phenomenon is attributed to the coating's effective reduction of battery polarization. Furthermore, the PE@AF-ZrO_2 pouch cell retains 98.1% energy after 200 cycles at 0.5C, whereas the bare PE pouch cell retains 96.2% (Fig. 6b). Moreover, when the cycle number reaches 1200, the PE@AF-ZrO_2 separator enables the cell to achieve an impressive energy retention rate of 93.5%, which demonstrates that PE@AF-ZrO_2 separator significantly enhances the cycle performance of lithium-ion batterie. Considering that both aramid and zirconia are commercially available, PE@AF-ZrO_2 separator exhibits commercial application potential.

4. Conclusion

In summary, by utilizing biomass-based aramid and zirconia, we propose a novel construction scheme for battery separators. The obtained PE@AF-ZrO_2 composite separators show excellent electrolyte wettability (contact angle: 7.57°), electrolyte uptake ability (371%) and good thermal stability (expose at 130 °C for 1 h without obvious contraction). Moreover, the ionic conductivity of PE@AF-ZrO_2 composite separators achieved 0.306 mS cm^{-1}, the polarization voltage of the battery has been significantly reduced to 0.36 V, as a result, endowing LFP battery with excellent rate and cycle performance, specifically such as 128.2 mAh g^{-1} discharge specific capacity at 10C, 93.5% energy retention after 1200 cycles. The synergistic design of the PE@AF-ZrO2 separator combines biomass-derived aramid nanofibers (for high dielectric strength and mechanical strength) and zirconia nanoparticles (for high puncture resistance and thermal stability). This design not only achieves an excellent balance between structural robustness and electrochemical performance but also offers a valuable reference for developing separators with high strength, high puncture resistance and low internal resistance—properties critical for next-generation lithium-ion batteries (LIBs).

Author contributions

D. Y. conceived the idea and written the manuscript and designed the electrochemical tests. All of the authors contributed to the general discussion and reviewed the manuscript.

Conflicts of interest

The authors declare no conflict of interest.

Data availability

All data included in this study are available upon request by contact with the corresponding author.

Supplementary information is available: The characterization data of aramid fibers, zirconia, and the pore size data of the separator can all be found in the SI section. See DOI: **https://doi.org/10.1039/d5ra03903g**.

Acknowledgements

We gratefully acknowledge the financial support from the Science and Technology Project of State Grid Corporation of China under Grant 5108-202218280A-2-76-XG.

References

1 B. Yuan, K. Wen, D. Chen, Y. Liu, Y. Dong, C. Feng, Y. Han, J. Han, Y. Zhang, C. Xia, A. Sun and W. He, *Adv. Funct. Mater.*, 2021, **31**, 2101420.
2 N. Lingappan, W. Lee, S. Passerini and M. Pecht, *Renewable Sustainable Energy Rev.*, 2023, **187**, 113726.
3 X. Zhang, Q. Sun, C. Zhen, Y. Niu, Y. Han, G. Zeng, D. Chen, C. Feng, N. Chen, W. Lv and W. He, *Energy Storage Mater.*, 2021, **37**, 628–647.
4 Y. Wang, X. Liu, J. Sheng, H. Zhu and R. Yang, *ACS Sustain. Chem. Eng.*, 2021, **9**, 14756–14765.
5 X. Zhang, J. Li, K. Qi, Y. Yang, D. Liu, T. Wang, S. Liang, B. Lu, Y. Zhu and J. Zhou, *Adv. Mater.*, 2022, **34**, e2205175.
6 Y. Min, L. Guo, G. Wei, D. Xian, B. Zhang and L. Wang, *Chem. Eng. J.*, 2022, **443**, 136480.
7 Y. Li, G. Zhang, B. Chen, W. Zhao, L. Sha, D. Wang, J. Yu and S. Shi, *Chin. Chem. Lett.*, 2022, **33**, 3287–3290.
8 X. Huang, R. He, M. Li, M. O. L. Chee, P. Dong and J. Lu, *Mater. Today*, 2020, **41**, 143–155.
9 Q. Song, A. Li, L. Shi, C. Qian, T. G. Feric, Y. Fu, H. Zhang, Z. Li, P. Wang, Z. Li, H. Zhai, X. Wang, M. Dontigny, K. Zaghib, A.-H. Park, K. Myers, X. Chuan and Y. Yang, *Energy Storage Mater.*, 2019, **22**, 48–56.
10 M. A. Taha, G. Sudre, A. Radulescu, F. Gouanvé, M. Fumagalli, T. Chaussée, V. Bounor-Legaré and R. Fulchiron, *ACS Appl. Energy Mater.*, 2025, **8**, 1282–1291.
11 Y. S. Jung, A. S. Cavanagh, L. Gedvilas, N. E. Widjonarko, I. D. Scott, S. H. Lee, G. H. Kim, S. M. George and A. C. Dillon, *Adv. Energy Mater.*, 2012, **2**, 1022–1027.
12 X. Gao, L. Sheng, M. Li, X. Xie, L. Yang, Y. Gong, M. Cao, Y. Bai, H. Dong, G. Liu, T. Wang, X. Huang and J. He, *ACS Appl. Polym. Mater.*, 2022, **4**, 5125–5133.
13 M. M. Rahman, S. Mateti, Q. Cai, I. Sultana, Y. Fan, X. Wang, C. Hou and Y. Chen, *Energy Storage Mater.*, 2019, **19**, 352–359.
14 X. Shen, L. Zhang, J. Zhu and X. Duan, *Energy Storage Mater.*, 2025, **80**, 104389.
15 P. Jing, M. Liu, P. Wang, J. Yang, M. Tang, C. He, Y. Pu and M. Liu, *Chem. Eng. J.*, 2020, **388**, 124259.
16 M. Guo, Y. Wang, W. Wang, F. Li, G. Ye, Y. Yan, P. Qi, K. Luo and R. Wang, *ACS Appl. Nano Mater.*, 2025, **8**, 10568–10582.

17 Y. Suharto, Y. Lee, J.-S. Yu, W. Choi and K. J. Kim, *J. Power Sources*, 2018, **376**, 184–190.
18 Q. Deng, X. Chuan, Y. Zhao, F. Liu, S. Huang and J. Wu, *RSC Adv.*, 2024, **14**, 16912–16920.
19 M. Makki, G. Ayoub, C. W. Lee, C. Bae and X. Colin, *Polym. Degrad. Stab.*, 2023, **216**, 110469.
20 J. Li, L. Chen, F. Wang, Z. Qin, Y. Zhang, N. Zhang, X. Liu and G. Chen, *Chem. Eng. J.*, 2023, **451**, 138536.
21 Y. Li, P. Li, X. Lan, Y. Jiang and X. Hu, *Mater. Today Phys.*, 2023, **38**, 101256.
22 S. Grira, M. Alkhedher, H. Abu Khalifeh, M. Ramadan and M. Ghazal, *Bioresour. Technol.*, 2024, **394**, 130225.